RSC Advances

PAPER

View Article Online
View Journal | View Issue

Cite this: *RSC Adv.*, 2025, **15**, 12563

A high-temperature optical cell for chemical analysis of vapor using combined spectroscopy approaches

Robin Roper,[a] Ruchi Gakhar, *[a] Alejandro Ramos Ballesteros[a] and Ammon Williams *[b]

This paper introduces a novel optical cell design that integrates ultraviolet-visible (UV-vis) and laser-induced breakdown spectroscopy (LIBS) for comprehensive vapor phase chemical analysis at temperatures up to 450 °C. The motivation behind this research is to overcome the limitations of existing vapor phase spectroscopy techniques by providing a versatile and efficient solution for detailed chemical analysis in high-temperature environments. The modular design of the optical cell enables the optimization of optical path length and beam diameter to meet the specific requirements of each spectroscopy technique. Experimental results demonstrated good resolution when analyzing both organic (naphthalene) and inorganic ($SbCl_5$) vapors. A key innovation discussed is the implementation of a cover gas buffer to prevent material buildup on the optical windows, ensuring the integrity and longevity of the cell during extended operation. This approach enhances the capabilities of existing techniques and extends their applicability to various scientific and industrial applications, including environmental monitoring, pharmaceuticals, materials science, and chemical manufacturing.

Received 28th February 2025
Accepted 4th April 2025

DOI: 10.1039/d5ra01462j

rsc.li/rsc-advances

1 Introduction

The demand for advanced vapor spectroscopy capabilities has grown significantly for studying high-temperature processes and reactions—such as those in combustion, metallurgy, and nuclear science—where traditional analytical methods may not be feasible. These tools are essential for analyzing reaction intermediates and volatile compounds.

Various analytical techniques are commonly employed to study vapors and gases. Gas chromatography (GC) is often paired with mass spectrometry (MS) or Fourier-transform infrared spectroscopy (FTIR) for compound identification. A limitation of GC is that it is often temperature limited and sensitive to particulates in the sample gas. FTIR analyzes the vibrational properties of various functional groups and bonds by identifying specific molecular vibrations within the infrared spectrum. This technique allows for the identification and analysis of the chemical composition and structure of a sample based on the unique vibrational frequencies of its molecular bonds. A challenge with FTIR is limited sensitivity and potential interferences from background gases. Photoionization detectors (PID) ionize gases and monitor the resulting current, while flame ionization detectors (FID), typically coupled with GC, measure ions formed during the combustion of organic compounds. PID has a low dynamic range and is not sensitive to alkanes and high ionization potential compounds while FID cannot detect inorganic compounds or permanent gases. Electron capture detectors (ECD), also paired with GC, detect electronegative compounds (such as halogens, nitrates and organometallics) by monitoring changes in current due to electron absorption but is not effective in other gas matrixes. Optical emission spectroscopy (OES) analyzes light emitted by excited atoms or molecules, and Raman spectroscopy is another vibrational technique used to identify polarized bonds. While OES is suitable for many analytes, sample preparation is challenging, and careful matrix matching is needed. Raman generally has low sensitivity but may be effective for some molecular vapors and gases.

Additionally, many of these techniques are destructive, and only a few allow for rapid, *in situ*, or in-line analysis with minimal system disturbance and flexibility in experimental setup. This highlights the necessity to develop an experimental arrangement that offers the required adaptability for continuous, rapid, and in-line coupling measurements. It is evident that the integration of techniques is crucial for gas analysis, and an unexplored option is the combination of ultraviolet-visible spectroscopy (UV-vis) and laser-induced breakdown spectroscopy (LIBS), given their precision and sensitivity. This combination of absorption and emission spectroscopy provides valuable information for understanding the composition and chemical behavior of gases. Furthermore, when developed for

[a]*Advanced Technology of Molten Salts, Idaho National Laboratory, Idaho Falls ID 83415, USA. E-mail: ruchi.gakhar@inl.gov*

[b]*Material Minimization, Security & International Safeguards, Idaho National Laboratory, Idaho Falls ID 83415, USA. E-mail: ammon.williams@inl.gov*

in-line analysis, it avoids unnecessary sample treatment that could alter the nature or chemical state of the vapors. Applying these technologies to the vapor phase can provide critical insights in various scientific and industrial applications, including environmental monitoring, pharmaceuticals, materials science, and chemical manufacturing. This combinatorial in-line chemical monitoring technique is also valuable for molten salt energy conversion technologies (off-gas systems), where the harsh environments of radiation and temperature present significant challenges. It should be noted that other combinations of analytical techniques may also be beneficial based on the specific gas/vapor sample. However, the focus of this work is the combination of LIBS and UV-vis.

UV-vis spectroscopy is widely used for determining absorption characteristics, providing information about electronic structure and concentration of substances. This technique is useful for monitoring the concentration of pollutants in air and water, analyzing the purity of chemical reagents, and studying the kinetics.[1,2] The ability to obtain real-time data makes UV-vis spectroscopy indispensable for process control and quality assurance in nuclear and industrial applications.[3,4] LIBS enables rapid elemental analysis of solid, liquids or gases by generating plasma from the sample and analyzing the emitted light during de-excitation.[5] This versatile technique requires minimal sample preparation and delivers fast results, making it suitable for applications in environmental monitoring,[6] forensic analysis,[7] and industrial quality control.[8] Furthermore, LIBS can detect trace elements with high sensitivity, which is crucial for identifying contaminants in food,[9] pharmaceuticals,[10] and nuclear materials.[11] In the nuclear industry, it is particularly valuable for measuring actinides,[12–14] including isotopic distributions.[15,16]

The literature on vapor phase spectroscopy is extensive, with numerous studies highlighting the benefits and applications of UV-vis and LIBS spectroscopy. LIBS has been used to study compounds in the vapor phase across various fields.[17–24] For instance, Dumitrescu *et al.*[17] developed a system to measure methane-air levels in combustion chambers, and Henry *et al.*[18] designed a gas phase LIBS system to measure carbon and hydrogen, both with and without the addition of helium. In the context of actinides, a noteworthy example is the system developed by Chan *et al.*[19,20] to measure gaseous UF_6. Similarly, gaseous species have been characterized by UV-vis studies.[25–37] DeKock and Gruen[25] measured gaseous transition metal chloride compounds at 1000 °C, determining electronic absorption spectra for VCl_2, $CrCl_2$, $FeCl_2$, $CoCl_2$, $NiCl_2$, and $CuCl_2$. Gruen and McBeth[26] used UV-vis spectroscopic techniques to characterize the complexation behavior of UCl_5 and UCl_4 with Al_2Cl_6. Boghosian *et al.*[28] determined molar absorptivities for lanthanide halides, which included chloride, bromide, and iodide compounds.

In this study, antimony (Sb) is used to evaluate the performance and efficiency of the developed experimental setup, necessitating a review of related literature on this element. Gregory *et al.*[37] reported the absorption spectra of antimony trichloride ($SbCl_3$) and antimony pentachloride ($SbCl_5$) in the vapor phase, as well as in mixtures with other halides. They conducted their measurements in sealed cells to prevent condensation at high temperatures, using a Cary 14H spectrometer. The chemistry of Sb has been extensively explored in solid and liquid phases using LIBS,[38–42] however, none were conducted with Sb in a chloride form and only one involved the gaseous phase.[41] In the study involving the gas phase, Simeonsson and Williamson[41] used a hydride generation approach to extract volatile species from solution for trace measurements in gas phase and reported a limit of detection (LOD) of 0.2 ppm in Ar gas using the Sb I 252.860 nm line.

Despite their extensive use, UV-vis and LIBS spectroscopy have traditionally been applied individually and have not been combined into a single apparatus. Integrating these spectroscopy approaches into one cohesive system can provide a powerful tool for comprehensive chemical analysis, enabling more detailed and accurate studies of vapor phase chemical species. The effective integration of these methods into a single, versatile apparatus is challenging since each technique has its own unique requirements and constraints regarding optical path length, beam diameter, focal length, and sample interaction volume. For instance, UV-vis spectroscopy requires an optical path for chromatic light transmission into and out of the cell while optimizing the optical path length through the sample. LIBS on the other hand, necessitates access to the cell with monochromatic laser light being focused through the cell window and into the vapor phase to generate plasma, and then the collection of chromatic light exiting the cell from the plasma location. These differing requirements must be considered when developing suitable cell geometries, windows material/coating selection, and likely necessitate independent optical paths and access points tailored for each measurement technique. Additionally, potential interferences between the different spectroscopy approaches may exist. For example, scattered light from the LIBS plasma could distort the transmission and absorption signal for UV-vis. Alternatively, scattered chromatic light from UV-vis has the potential to be collected as part of the LIBS spectrum, potentially introducing additional background to the measurement. While careful selection of optical paths, optics, and LIBS plasma location can mitigate or reduce these interactions, a better approach may be to time synchronize the two measurements so overlap with respect to time does not occur. This can be accomplished simply with the use of a digital delay generator (DDG) that controls/triggers the LIBS and UV-vis data acquisition with suitable delays between measurements.

The design and implementation of an optical cell tailored for combined UV-vis and LIBS spectroscopy are essential for advancing vapor phase chemical analysis. In this paper, a novel design of an optical cell that integrates UV-vis and LIBS spectroscopy for comprehensive vapor phase chemical analysis, is presented. The design accommodates the unique constraints imposed by each spectroscopic method and offers a versatile solution that can be adapted for various analytical needs. The versatility of design is leveraged by a modular approach, allowing for the modification and optimization of optical path length and beam diameter, which is crucial for accommodating the different requirements of UV-vis and LIBS spectroscopy.

This novel approach not only enhances the capabilities of existing spectroscopy techniques but also opens new avenues for research and development in chemical analysis.

2 Optical cell design & testing methods

2.1 Design considerations and parameters

Before delving into the detailed description of the optical cell and its design, it is crucial to understand the unique constraints that each spectroscopy approach—LIBS and UV-vis—imposes on the cell geometry. These constraints are fundamental in shaping the overall design. For LIBS, both excitation (laser light into the cell) and light collection (out of the cell) can occur through the same window or through separate windows.

UV-vis spectroscopy is performed in transmission mode, where a portion of the light (wavelength dependent) is absorbed in the sample, and the unabsorbed or transmitted light is collected by the spectrometer. The distance the light passes through the sample is known as the path length. In the simplest UV-vis setup, a straight-through geometry is used: light passes through the sample in one direction, with the light source on one side and light collection optics on the other. This setup requires at least two windows on the optical cell to allow for light transmission through the cell. Alternate UV-vis configurations include a multi-pass cell that uses mirrors to reflect the light through the cell multiple times.

The quality of the UV-vis signal is dependent on several factors, most importantly the optical path length, and the beam diameter. Optimizing these parameters improves the signal quality; however, the optimal values for salt species in vapor phase are not well-documented in literature. Therefore, experimental exploration of the optical path length and beam diameter was necessary to determine the optimized values for the vapor cell for these species. The configuration explored in this design was a straight through geometry with two optical windows.

2.2 Cell design and instrumentation

With the above in mind, a modular optical cell was designed, with which parameters such as optical path length and beam diameter could be experimentally explored to narrow the design space for probing vapor phase constituents. Fig. 1 shows the optical cell design. Here, 38.1 mm (1.5 inch) diameter uncoated UV Fused Silica windows (Thorlabs, VPW42) were used to obtain an optical window opening approximately 30 mm in diameter into the cell. These windows were uncoated to allow for better transmission of chromatic light from UV-vis and the LIBS plasma. The windows were sealed by sandwiching them between an outer stainless-steel ring and grafoil gaskets (Curtiss-Wright/AP Services, AP Style 6300L) as shown in Fig. 1b. Three screws (8–32) were used to tighten down and compress the gasket. This sealing approach allowed the cell to be rapidly disassembled and re-assembled as needed.

The cell body was a 2-inch (50.8 mm) outside diameter (OD) stainless steel tube fitted with the window end caps. With this design, the cell body could be replaced with tubes of varying lengths to meet specific measurement needs with defined optical path lengths. To test and optimize the optical path length for the current application, two tube sizes were used: 7.9 cm and 15.9 cm to obtain optical path lengths of 10 cm and 18 cm, respectively. The 18 cm length was dictated by the size of the tube furnace used to heat the cell. In other applications, the cell could be made longer as needed. The end caps consisted of the window seals described above as well as a clamping mechanism to make a seal with the outside surface of the stainless-steel tube body. A cross-sectional view of the end cap and the clamping mechanism is shown in Fig. 1b. Two grafoil gaskets (Curtiss-Wright/AP Services, custom cut) were compressed between the two angled jaws in the endcap *via* screws that draw the jaws together. This compression action forces the gaskets inward to tightly engage the outside surface of the stainless-steel tube, creating a seal. This design is typically used when sealing metallic components to quartz tubing and usually utilizes a rubber O-ring or gasket rather than a carbon based grafoil seal. Each end cap had a 0.25-inch (6.35 mm) OD tube that was welded to the inside jaw of the endcap and allows for gas inlet and outlet from the optical cell.

The entire cell, including the grafoil gaskets, were rated to temperatures as high as 450 °C in oxidizing environments and 600 °C under inert conditions. This allows for a range of different chemicals that can be tested. The tube furnace utilized in these initial tests was an MTI Corp, OTF-1200X. Initial testing with the vapor cell in the furnace showed a significant thermal gradient between the center of the optical cell and the windows.

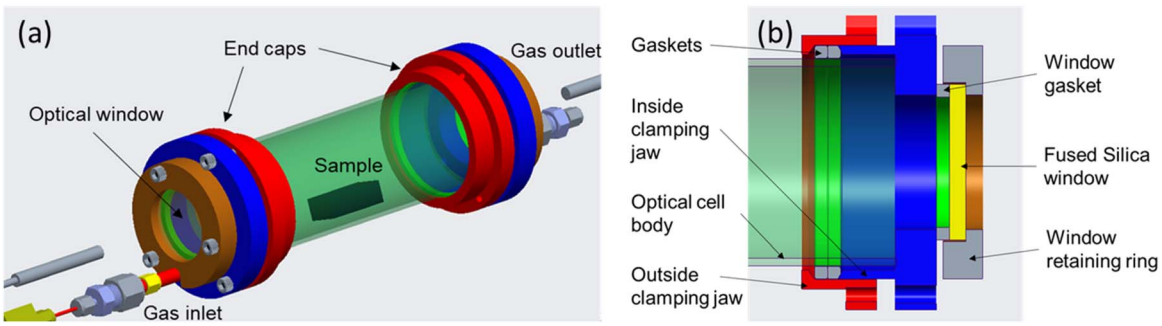

Fig. 1 (a) Framework of the versatile optical cell, and (b) expanded view of the window assembly.

For example, with the 18 cm path length vapor cell at a temperature of 450 °C (measured *via* the furnace control thermocouple at the center of the furnace, exterior to the cell), the windows were at ~210 °C (measured using an external thermocouple in contact with the window) due to increased heat loss at the windows and the edge of the furnace. As a result, material loaded into the cell at its center would boil and migrate towards the colder windows, where it could condense or freeze depending on the operating temperature of the furnace and the sample being measured. The large thermal gradient from the center of the cell to the windows is difficult to change in this setup. To address this issue, an external sample cell/chamber was developed, as shown in Fig. 2, which could be heated independently from the optical cell. This design allowed the optical cell to operate at significantly higher temperatures while still introducing the sample at a lower temperature. By increasing the optical cell temperatures such that the windows were above the boiling point of the sample, condensation and freezing on the windows was significantly reduced. The sample chamber consisted of 1-inch stainless steel tubing connected *via* Swagelok fittings. The chamber was wrapped with heat tape and then covered with a silicone sheet for insulation. Despite the availability of the external sample chamber, some tests were performed by adding the sample directly to the optical cell for simplicity during testing.

On either side of the optical cell and external sample chamber were high temperature valves (Swagelok, Model #SS-3NBS4-BKP-G) that could be opened or closed. The primary function of the valves was to allow for loading and unloading of the sample and optical cell in an inert atmosphere environment (glovebox). Once the sample was loaded, the optical cell, with closed valves, could be transferred out of the inert atmosphere to the furnace, connected to the gas lines without exposing the sample to air. The gas panel was configured with a two-way valve toggled between argon gas flow or vacuum (*via* a venturi), such that the cell could be evacuated and backfilled to ensure a clean atmosphere before testing, operated under vacuum, or under inert gas flow conditions. If the valves were closed at the onset of the experiment and remain closed, pressure in the cell would build with heating and the vapor phase within the cell could reach equilibrium vapor pressures under the temperature and pressure conditions. If the valves were left open, then gas flow from the gas panel could continuously pass through the cell and to the exhaust system.

The laser used for this work was a Nd:YAG laser (Quantel USA, Q-Smart 450) operating at 1064 nm. In this configuration, a z-pattern of mirrors was used to align the laser beam through a beam splitter (to reduce the energy), allowing for the laser to operate at a higher energy while minimizing instabilities and utilizing lower energies at the sample. After the beam splitter, the laser beam was directed through another set of mirrors in a z-pattern to achieve the correct height and orientation for the beam. The selection of the laser focusing lens and beam diameter is critical for gas applications. With longer focal lengths, the beam diameter passing through the window might be small enough to exceed the damage threshold of the window material. Additionally, Morgan *et al.*[24] found that if the focal length is too long, an elongated hourglass shaped plasma, which is cooler than optimal, occurs. If the focal length is extended further, there is insufficient energy for gas breakdown to occur. For a beam diameter of 6 mm (the incident beam diameter from Q-Smart 450), the ideal focal length was 35 mm. At this short focal length, it is challenging to work around the windows and constraints posed by the furnace, insulation, and other fixtures. To achieve a more practical focal length of between 125–140 mm, the laser beam diameter increased to 17.3 mm using a 2.66× beam expander.

The 2.66× beam expander utilized two optical components. The first was a concave lens with −75 mm focal length, and the second was a plano-convex lens with a 200 mm focal length, positioned 125 mm from the first lens. The first lens expanded the laser beam and the second lens collimated it into approximately a 17.3 mm diameter beam. A 2-inch laser mirror redirected this beam towards the optical cell. The laser beam was then focused into the optical cell using a 125 mm plano-convex lens (Thorlabs, LA4236), positioned about 80 mm from the

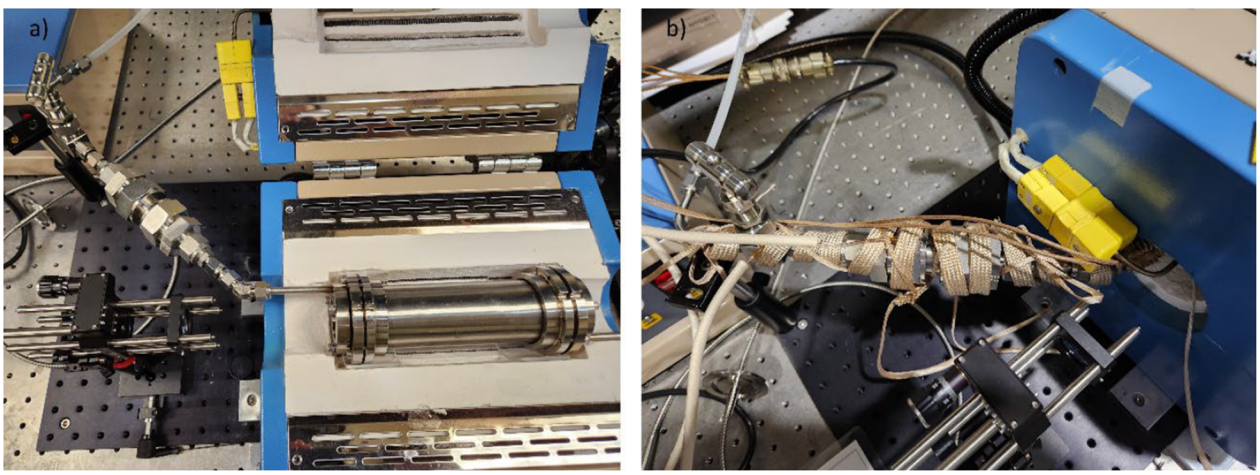

Fig. 2 (a) Picture of the external sampling chamber without the heat tape and (b) a photo of the external sample chamber with added heat tape before wrapping with silicone insulation tape.

optical cell window, resulting in a beam diameter of approximately 5.76 mm at the window surface. The plasma light collection was achieved using a 5 mm diameter fiber optic micro-collimator (Fiberguide, NA 0.22) connected to a kinematic mount positioned beside the 125 mm focusing lens. A SMA fiber optic cable (Ocean Optics, P400-5-UV-VIS) linked the micro-collimator to an Echelle spectrometer (Catalina Scientific, EMU 120/65). Two different EMU 120/65 spectrometers with distinct gratings were used. The first spectrometer grating, IX2:VIS/NIR, covered a spectral range from 350 nm to 950 nm with an average resolving power of 51 000 at 435 nm, and employed a Falcon 285 electron multiplying charge coupled device (EMCCD) detector from Raptor Photonics. The second spectrometer grating, UVU3:UV/VIS/NIR, spanned a spectral range from 200 nm to 1000 nm with a resolving power of 15 000 at 435 nm, and used an iXon3-885 EMCCD detector from Andor Technologies. Since neither detector had a digital shutter, a separate DDG (Quantum Composer, 9200) was utilized to gate delay the spectrometer. The gate delay varied in this study while the gate width was maintained at 80 μs. In the optical setup described above, the components following the beam expander were mounted on a breadboard platform (Thorlabs, 0.5-inch by 4-inch by 6-inch) attached to a rail (Newport, PRL-24). During LIBS measurements, the platform was positioned using a stop on the rail and secured. While performing UV-vis measurements, the breadboard platform was slid along the rail to clear the UV-vis beam path. As a result, time synchronization was not necessary between the LIBS and UV-vis measurements.

The UV-vis spectroscopy system coupled with the vapor cell comprises a high-resolution spectrometer (Ocean Optics HR6 utilizing a CCD array detector) with a range of 185–1100 nm, and a Deuterium-Halogen UV-vis-NIR light source (DH-2000-Bal) capable of illuminating from 190–2500 nm. Data transfer utilized High-OH fiber optic cables (Fiberguide, core diameter 400 μm, NA 0.22) with minimal attenuation over a range of 190–1250 nm. Data collection was performed using the OceanView software, set to 20 scans per collected spectrum, with integration times between 400–800 μs. The UV-vis setup included the central optical cell, previously described, and telescopic modules on both sides of the central cell. The telescopic modules were designed to provide flexibility in modifying the optical path length and beam diameter according to the sample's absorption characteristics, while being robust enough to require minimal adjustments without losing alignment. The optical path length can be adjusted to various lengths according to the sample's absorption cross-section and concentration by exchanging the central cell body (tube) and fitting the same side windows. The telescopic units consist of plano-convex lenses that amplify the light beam from the illumination source (point source from the fiber guide) to increase the effective interaction volume with the sample along the cell. On the opposite side (outlet), the other telescopic unit reduces the collimated beam at the focal point, which is the fiber guide that transmits the photons to the spectrometer. The beam size is determined by the choice of lens and its focal length (directly related to the lens diameter). Two sets of collimating/receiving lenses were used: 30 mm and 50 mm focal lengths. The lenses are positioned in the apparatus so that the distance between the SMA connector of the optical fiber and the vertical axis of the lens matches the focal length. The 50 mm and 30 mm lenses generate beam diameters of 22 mm and 11 mm, respectively. The mounts for each type of lens are adjusted according to the lens diameter. The total optical path between the light source and the receiving fiber optics was adjusted by moving the receiving optics along a rail. The available range for total optical path distance adjustments was approximately 57 to 73 cm. Two different systems (one organic, naphthalene, and one inorganic, $SbCl_5$) were tested to evaluate the detection and behavior of the experimental setup.

2.3 Chemicals

Naphthalene ($H_{10}C_8$, Sigma-Aldrich, 99% purity) was selected for vapor-phase analysis due to its low sublimation temperature (~80 °C), its high molar absorption coefficient and its characteristic absorption in the UV range.[43] The parameter optimization of the UV-vis design configuration, including path length, beam diameter, and optical path (the distance between optical mounts on either side of the furnace), was performed using naphthalene at 85 °C, just above its sublimation temperature. The spectrum for naphthalene was also collected at 450 °C to assess the effect of temperature on the resolution and sensitivity of the spectroscopic cell. For each test, approximately 0.6 g naphthalene crystals were weighed and loaded into the vapor cell using a high-precision analytical balance (Mettler Toledo XPE504).

After refining the optical cell parameters for the UV-vis design and conducting high-temperature testing, a volatile metal halide system, antimony pentachloride ($SbCl_5$, boiling point 140 °C, Thermo Fisher 99.997% purity, lot number 017570-14), was selected to demonstrate the applicability of this cell for molten salt vapor phase analysis. $SbCl_5$ is a highly volatile and reactive salt that decomposes upon heating, releasing toxic and corrosive vapors such as chlorine gas (Cl_2) and antimony trichloride ($SbCl_3$) in absence of air. In the presence of air, it decomposes to antimony oxide (Sb_2O_5) and Cl_2. HSC chemistry software[44] was used for Gibbs energy calculations for these reactions. The decomposition of $SbCl_5$ in the presence of oxygen is highly likely at any temperature, and the decomposition without the presence of oxygen is likely above approximately 200 °C.

The glovebox was maintained below 0.1 ppm O_2 and H_2O levels to ensure an inert and controlled environment. Approximately 0.9 g of liquid $SbCl_5$ was placed into a glass vial using fluorinated pipettes, which was then loaded into the apparatus. The sample was then transferred into the optical cell within the glovebox to maintain the integrity of the sample. The vapor cell was then sealed to reduce contamination or loss of sample due to chemical reactions. The sample chamber was heated to 140 °C, to allow the vaporization of $SbCl_5$. The optical cell was heated to 350 °C to prevent condensation of $SbCl_5$ on the windows (windows temperatures were 169 °C). Spectra were collected while maintaining this temperature for up to 3.5 hours to evaluate the effect of $SbCl_5$ concentration and its corresponding spectrum.

3 Results and discussions

3.1 Optimization of test configuration

Initial pressure testing of the optical cell was conducted to explore the effectiveness of the design and seal mechanisms. Initially, the seals were not sufficiently tight to hold pressures greater than 5 psi. However, after torquing the bolts to their max torque rating of 2.25 Nm (~20 lb-in), the leaks were significantly reduced but not eliminated. The leaks were typically located where the end caps were connected to the 2-inch cell body. This seal type is better suited for rubber O-rings rather than the grafoil seals for use at high temperatures. As a result, for tests at temperatures lower than 288 °C, PTFE O-rings were used which eliminated leaking at this location. The seal around the windows also had a slight leak in between the bolt pattern, which was improved by further tightening the bolts but was not eliminated in all cases. With all grafoil seals, the leak rate was measured to be approximately 0.2 psi per minute at 10 psi. While this leak rate was deemed sufficient for flowing applications where the operating pressures were at ambient conditions, it is too high for testing in a sealed system where the pressures could be much greater than 10 psi. Indeed, initial tests using naphthalene in a closed configuration resulted in a strong naphthalene smell, indicating loss of material *via* leaking (pressure measurements in the cell in closed configurations were not possible due to the potential for material freeze out on the gauge). As a result, all future testing with this hardware was conducted in a flowing configuration with Ar gas at flows of approximately 1 L min^{-1}. To enhance the cell's sealing capability, it is recommended to use welds when possible and to utilize additional and stronger bolts to increase the compression of the grafoil seals.

With the optical cell pressure testing complete, testing of the UV-vis design parameters was carried out in a series of experiments using naphthalene at 85 °C. Naphthalene is a polyaromatic organic compound with characteristic transitions in the UV range due to conjugated double bonds. These transitions result in a fine structure that have been extensively studied due to their health impacts and environmental implications, particularly from the combustion of coal, oils, and gas in the chemical industry. Studies by Ferguson,[43] George,[45] Suto,[46] and Orain[47] have reported the absorption cross-section, fluorescence, and quantum yield in both the UV and visible spectra. The absorption spectrum of naphthalene consists of a series of peaks between 250–280 nm due to a second transition, which are complex and challenging to interpret due to conjugation. In 1957, Ferguson[43] reported the vapor spectra of naphthalene at 313 K with small amounts of argon to facilitate thermal equilibrium. It has become common practice in literature to use the absorption peak at 265 nm as a reference for concentration calculations. Orain[47] reported an absorption cross-section for 266 nm peak between 1.25–1.35 × 10^{-17} in the vapor phase.

Fig. 3a illustrates the electronic absorption spectra for naphthalene in vapor phase after 1 hour of heating with a set-point of 85 °C, varying two parameters: path length (10 and 18 cm) and beam diameter (11 and 22 mm) using the corresponding lenses. The relative position of the collimation lenses was tested by moving the receiving optical mount along a rail to increase distance between optics. A signal attenuation of 11.4% was observed after a distance increase of 16 cm. The sample mass and argon flow conditions were kept constant between tests; therefore, it is assumed that the vapor concentration between tests was the same. Flow configuration of the cell limits the determination of the actual concentration of the vapor species.

Optimal signal strength and peak resolution were achieved with a larger beam diameter and longer path length (22 mm beam, 18 cm path). The data indicates that beam size is the most critical factor for improving signal resolution and intensity. While increasing the path length enhances signal intensity, it does not necessarily improve resolution, as shown by the 11 mm × 18 cm and 11 mm × 10 cm configurations. A larger beam diameter expands the hypothetical measurement cylinder (interaction volume), allowing for more spatially distributed interactions. This can reduce self-absorption and energy transfer effects, potentially mitigating impact of scattering on spectral resolution. Smaller interaction volumes (narrower beams or shorter paths) generate weaker signals that are more susceptible to noise and fluctuations, degrading spectral feature resolution. Extending the path length increases photon absorption, while a larger beam diameter ensures more molecules contribute to the measured signal. This combination enhances peak definition, making absorption features more distinct relative to the baseline. Therefore, optimizing both beam size and path length improves measurement sensitivity and enhances the reliability of spectral analysis.

To further assess the effect of these parameters, the beam interaction volume was calculated from the beam diameter and path length. The absorption intensity at select wavelengths was compared between these beam interaction volumes. Table 1 shows the parameters and calculated beam interaction volumes, and some select wavelengths with corresponding intensities, and Fig. 3b shows the intensities *versus* beam interaction volume plot. Although the resolution is suboptimal, intensities *versus* beam interaction volume plot, Fig. 3b shows a general trend, supporting the hypothesis that a higher beam interaction volume will lead to a higher intensity signal.

3.2 High-temperature tests

The spectrum for naphthalene was collected at 450 °C to assess the functionality of the design with the addition of the external sample chamber. During the test, the optical cell was raised to 450 °C. Once the cell temperature stabilized, the sample chamber was raised to and maintained at 85 °C to vaporize naphthalene, and transfer into the optical cell. Fig. 4 shows the spectra recorded for naphthalene at 450 °C.

A change in the spectral features of naphthalene with temperature is notable. A similar effect has been observed by Grosch *et al.*,[48] where naphthalene was studied up to 500 °C using a similar experimental spectroscopic setup, albeit with a larger size and less flexibility. Grosch *et al.* reported the temperature-dependent changes in absorption spectra of

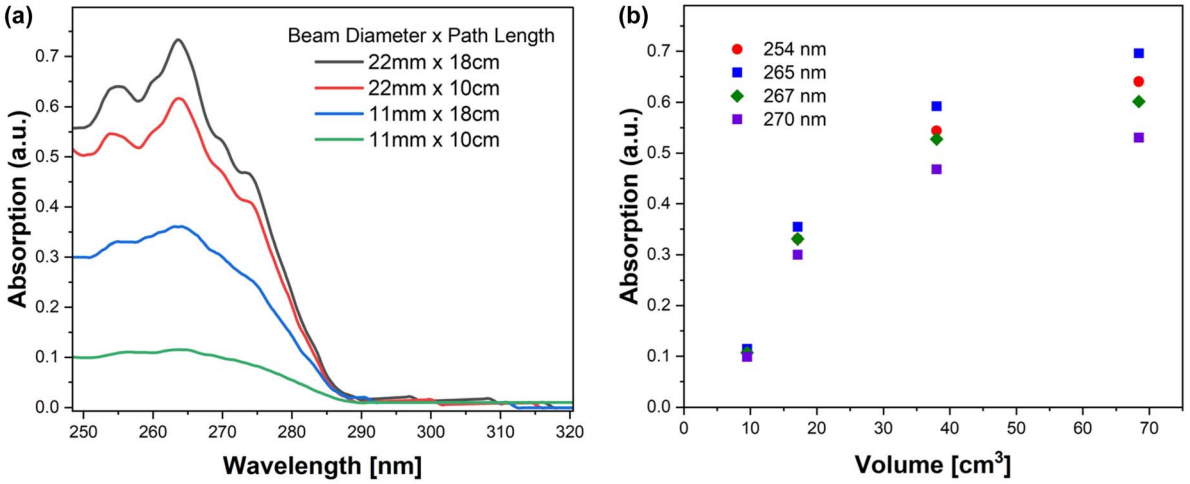

Fig. 3 (a) Average spectra of naphthalene vapor at steady-state at 85 °C. Beam diameter and path length were varied to determine optimal configuration. The strongest signal was observed at a 22 mm beam diameter and 18 cm path length. (b) Scatter plot of beam interaction volume and peak intensities at select wavelengths.

naphthalene, with the fine structure vanishing and the overall broadening of the peak. These observations can be explained by the presence and overlap of vibrational states, which create a continuum of absorption rather than the fine structure observed in the vapor phase at lower concentrations and temperatures.[48] Additionally, higher temperatures increase molecular motion, resulting in Doppler broadening and collisional broadening, which further contributes to the broadening of absorption peaks. These combined effects explain why the absorption peak shifts to lower energies (red shift) as temperature increases. This phenomenon has been also reported for benzene, naphthalene, anthracene, diphenyl, perylene, pyrene, phenanthrene, and triphenylene crystals show narrower and more intense signals in absorption spectra at low-temperature (−170 °C) compared to room temperature.[49] This observation indicates that interactions among aromatic hydrogens affect the shape of the absorption peaks. It is important to note the blue shift for naphthalene under Ar in this work compared to the spectrum reported by Grosch *et al.* under N_2.[48] This blue shift in the naphthalene spectra can be attributed to the weaker interactions and lower stabilization of the excited states in Ar compared to N_2, due to its lower polarizability compared to N_2. Additionally, Angus and Morris[50] conducted studies on solid solutions of naphthalene in noble gas matrices and found shifts in the characteristic absorption peaks depending on the matrix.

For naphthalene, LIBS measurements were also performed alongside UV-vis analysis. A typical LIBS spectrum of naphthalene and argon in the optical cell is shown in Fig. 5. This data was collected at 43 mJ with a gate delay of 2 μs and is the accumulation of 740 shots at 2 Hz. Many shots were

Table 1 Intensities of select wavelengths at each beam interaction volume

			Select points	
Beam diameter (cm)	Path length (cm)	Beam interaction volume (cm^3)	Wavelength (nm)	Intensity
1.1	10	9.50	254	0.10838
			265	0.11451
			267	0.10684
			270	0.09884
1.1	18	17.11	254	0.33070
			265	0.35461
			267	0.33092
			270	0.29998
2.2	10	38.01	254	0.54402
			265	0.59230
			267	0.52743
			270	0.46801
2.2	18	68.42	245	0.64065
			265	0.69601
			267	0.60166
			270	0.53033

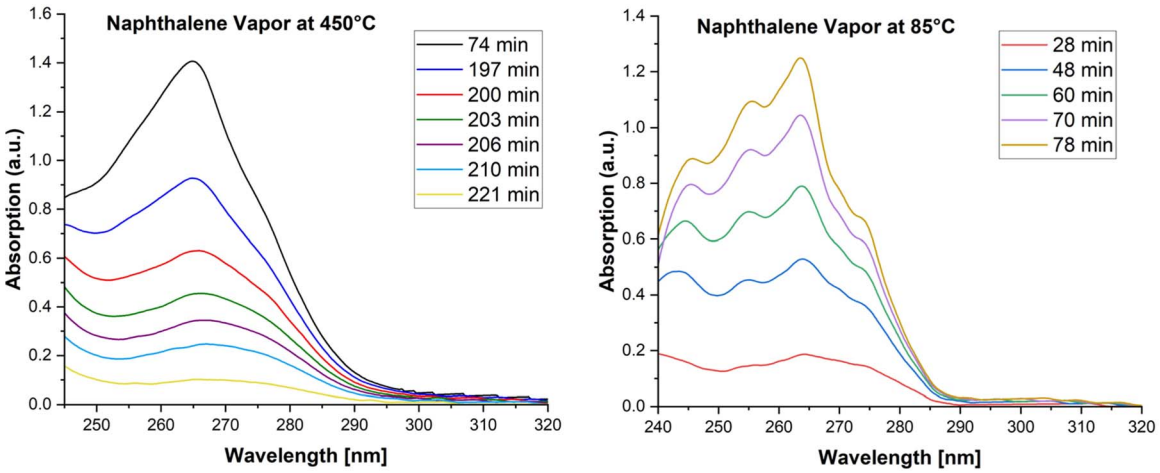

Fig. 4 (Left) Average curves for naphthalene vapor at 450 °C over time, showing sample depletion at the end of the test. (Right) Average curves for naphthalene vapor at 85 °C over time, showing the increase of naphthalene concentration at the start of the test.

accumulated since single shot data did not reveal any transients or trends within the timeframe of interest. Increasing shot accumulations resulted in lower noise and better detection of weaker spectral lines. In this measurement, the spectral range was from 350 nm to 950 nm. The signal was primarily dominated by the argon carrier gas, with most of the prominent lines originating from argon. The spectrum revealed several atomic lines for carbon (C), hydrogen (H), oxygen (O), and nitrogen (N). The presence of N and O suggest air infiltration in the system. LIBS measurements were performed on the Ar gas source in a smaller cell sealed with rubber O-rings and no indications of N or O_2 were present. As a result, it is assumed that the air leaking into the cell occured throughout the experiment through the sealing mechanisms of the cell and not due to initial contamination in the system or in the Ar carrier gas. Due to the long gate width (exposure time) of 80 μs used for this data collection, there was also signal from two molecular species, diatomic carbon (C_2) and cyanide (CN). However, the weakest of the C_2 and CN spectral lines only emerged statistically from the spectrum at higher shot accumulations, while the C lines and some of the CN lines were discernible in the spectra from single laser shots with signal to noise ratios (SNR) of approximately 2–3. Table 2 shows the lines identified for C, C_2 and CN using 740 shot accumulations. The most intense C bearing line was the CN line at 388.32 nm and the intensity of the other lines in the table are shown relative to this line. The presence of these molecular species is expected, as they are commonly reported in hydrocarbons in the presence of air.[51,52]

Also shown in Table 2 are the signal to background ratios (SBR) and the SNRs for each line reported. The SBR was calculated as the peak intensity divided by the background signal near the peak of interest. While this approach is simple and does provide a reasonable approximation of a line's strength, it overlooks the level of noise present in the background. To capture more of the noise information, the SNR was also calculated as the background intensity subtracted from the

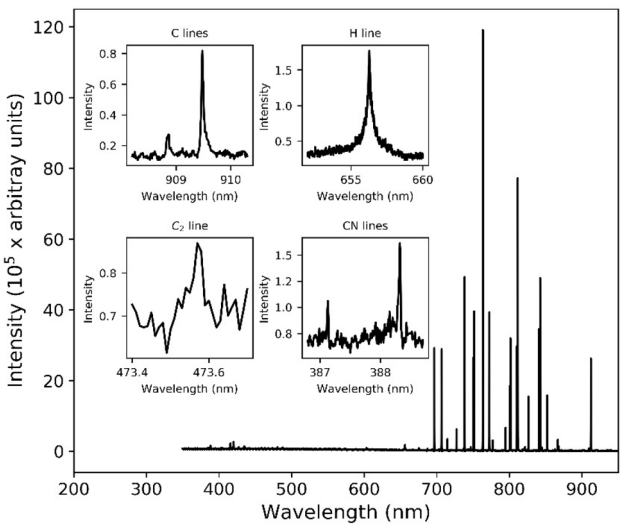

Fig. 5 A full LIBS spectrum from the optical cell in naphthalene vapor at 85 °C, including CN, H, C_2, and C lines at 2 us gate delay and 43 mJ. The spectrum is an accumulation of 740 shots.

Table 2 Observed spectral lines for C, C_2 and CN with their relative intensities, SBRs, and SNRs

Spectral line (nm)	Wavelength (nm)	Relative intensity	SBR	SNR
C I 909.48	909.48	0.51	5.50	58.84
C I 911.18	911.18	0.23	2.56	18.11
C I 908.85	908.87	0.17	1.86	10.54
C I 907.83	907.84	0.13	1.49	5.86
C_2 473.59	473.57	0.54	1.26	5.89
C_2 471.49	471.49	0.47	1.14	2.88
CN 388.32	388.32	1.00	2.34	20.86
CN 387.12	387.13	0.66	1.53	6.71
CN 385.44	385.45	0.58	1.25	2.86
CN 386.15	386.15	0.50	1.18	2.67

peak intensity, all divided by the standard deviation of the background signal.

Additional testing was conducted to evaluate long-term durability of the cell and optical system for an extended period while conducting measurements *via* LIBS and UV-vis. The cell with a 10 cm path length and a 22 mm collimated beam diameter, was loaded with 0.6 g of naphthalene. The temperature was maintained at 85 °C for up to 30 hours. The signal was observed to reach an equilibrium like those shown under the same conditions for UV-vis and LIBS. However, minor fogging was observed approximately four hours into the test, indicating a buildup of material on the windows. This deposit could not have been naphthalene condensation, as the windows were too hot to maintain naphthalene in solid or liquid form. It was likely a product of chemical reactions in the cell due to water and oxygen contamination, leading to material deposits or chemical etching of the quartz windows. This result suggests that simply maintaining the windows at high temperatures is not a viable long-term solution, necessitating alternative design innovations.

To mitigate the observed sample interactions on the windows, an alternative design was explored to limit material accumulation on the windows. The new concept was developed utilizing a cover gas buffer between the sample and the windows. Fig. 6 shows a schematic depicting a double-window design and how it would function with a laser for LIBS measurements. A primary window was used to seal the interior of the chamber, while a secondary internal window with a small hole (5 mm) was positioned 25 mm from the primary window. A cover gas was introduced between the two windows and into the main section of the optical cell through the hole bored in the secondary window. The gas flow is utilized to prevent the vapor in the main cell from flowing back into the small chamber, thereby protecting the exterior window from deposits. This design was intended as proof of principle. In future iterations, the secondary window could simply be replaced by an orifice through which both LIBS and UV-vis measurements are conducted.

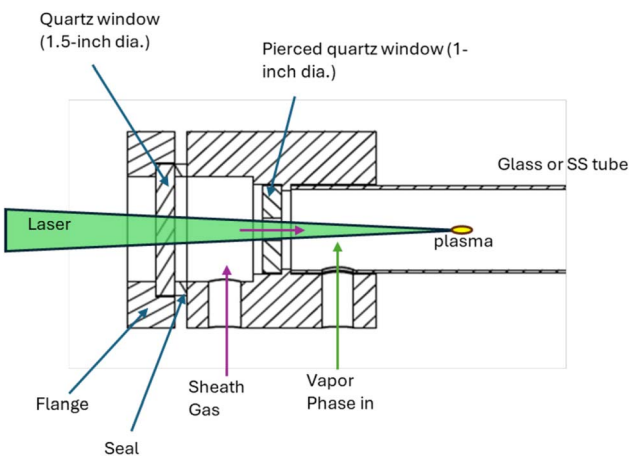

Fig. 6 Schematic of the double-window optical cell design.

This design was tested using a 3D printed optical cell made from Onyx as the material (operating temperature of 145 °C), with rubber O-rings, and quartz windows. The sample carrier gas was Ar, flowing at approximately ~1 L min^{-1}. In this setup, Ar was also used as the cover gas at a similar flow rate of about 1 L min^{-1}. Tests were conducted using naphthalene as a sample at temperatures between 90–100 °C to explore the signal and the longevity of the new concept. UV-vis measurements with a 11 mm diameter beam showed that the naphthalene signal was only marginally affected by the hole in the secondary window, and a clear naphthalene peak was observable as expected.

For LIBS, measurements were acquired using a spectral range from 200 nm to 950 nm, enabling the detection of the strong C line at 247.853 nm, which was not possible with the previous spectrometer configuration. The SBR and SNR for this line was 5.0 and 33.54, respectively. Unfortunately, the strong C lines in the 906–912 nm range observed previously fell into a spectral gap due to the echelle grating of this spectrometer. Strong H bands were also observable around 656.27 nm. Due to the low-temperature design of the cell, O-rings were used, and consequently there were no indications of O or N in the LIBS spectra.

Over a series of tests in the new 3D-printed design, the optical cell operated for a combined total of 44 hours, during which 1.6 g of sample passed through the optical cell without any interactions or observed material deposits on the windows. This marks a significant improvement over previous tests, where material deposits were observed after just 4 hours. This new prototype configuration with a cover gas proved effective at protecting the windows from material deposits and interferences in the spectroscopy measurements and is therefore recommended for future optical cell designs.

3.3 Molten salt vapor test: $SbCl_5$ species

A test with antimony(v) chloride ($SbCl_5$) was conducted using the high-temperature stainless steel optical cell in closed

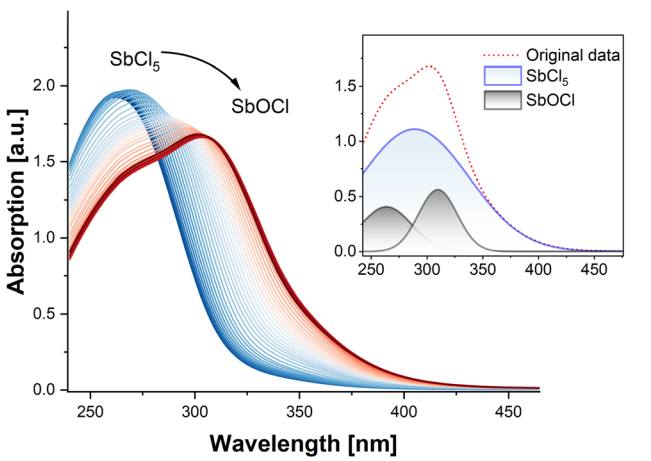

Fig. 7 UV-vis spectra of $SbCl_5$ vapor species, decomposed to $SbCl_3$ at 350 °C.

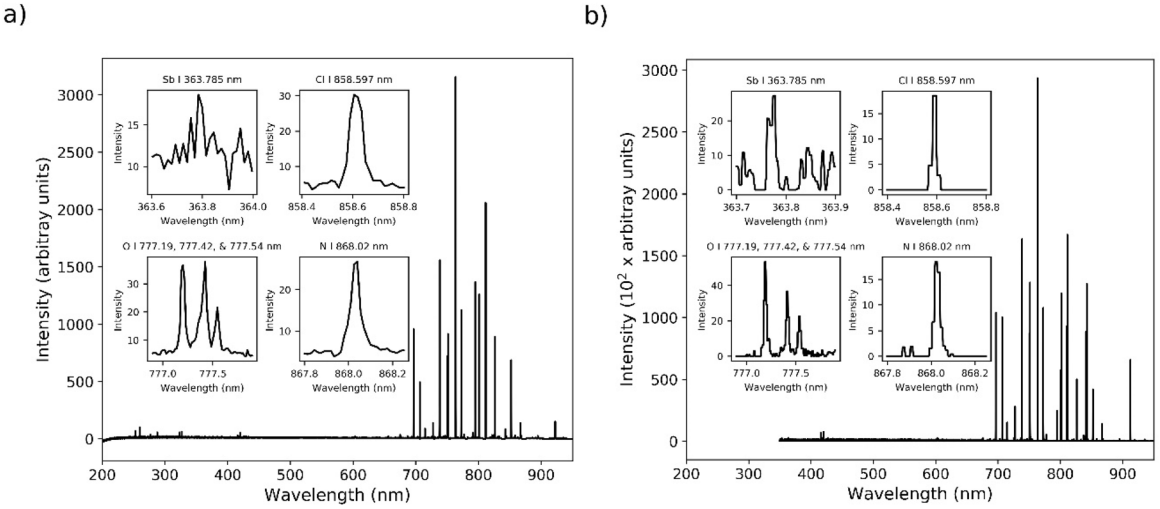

Fig. 8 LIBS spectra of $SbCl_5$ vapor in Ar gas. (a) Data from the 200–1000 nm spectrometer, taken at 28 mJ with a gate delay of 3 μs and is an accumulation of 20 shots, and (b) data from the 350–950 nm spectrometer taken at 26 mJ and 2 μs gate delay and is an accumulation of 120 shots.

configuration as a proof of concept at high temperatures for molten salt systems. In these experiments, the liquid $SbCl_5$ sample was heated to a temperature of approximately 140 °C in the external sample chamber, while the optical cell was maintained at a temperature of 350 °C. Under these conditions, the cell windows were at a temperature above the boiling point of $SbCl_5$, enhancing thermal decomposition to $SbCl_3$ and Cl_2.

Fig. 7 shows the UV-vis spectra obtained for $SbCl_5$ at 350 °C over a period of 5 hours. Initial peak observed (263 nm, blue curve) corresponds to the second absorption peak for $SbCl_5$, as reported by Gregory *et al.*[37] who observed two intense absorption peaks for $SbCl_5$ at 298 K, around 230 nm and 270 nm. In contrast, $SbCl_3$ exhibits one primary absorption peak below 200 nm with a shoulder at 255 nm with a low absorption coefficient. Over time, the 263 nm peak for $SbCl_5$ exhibits a bathochromic shift, in addition to the appearance of new bands. According to thermodynamic calculations, the most favored reaction involves the decomposition of $SbCl_5$ to $SbCl_3$, which is not observable either due to its rapid oxidation or its low absorption coefficient in the 250–350 nm range. The new bands (red curve) indicate the oxidation of decomposed Sb(III) species, resulting in the formation of SbOCl.[53] A closer examination of the red curve through deconvolution (inset, Fig. 7) reveals a broad absorption peak at 298 nm (blue) and two lower-intensity peaks (grey) at 263 and 309 nm. The two lower-intensity peaks can be correlated to the presence of SbOCl, as reported in aqueous systems,[53] while the broad peak at 298 nm might correspond to some unreacted $SbCl_5$ and unresolved more complex oxychloride species. Hu *et al.* (2024)[54] reported diffuse reflectance spectra for various $Sb_xO_yCl_z$ showing lower energy absorption for higher oxychlorides, indicating complexity of individual determination.

Table 3 Spectral lines for $SbCl_5$ observed using the 200–950 nm spectrometer. The intensity is shown relative to the strongest Sb line

Spectral line (nm)	Wavelength (nm)	Relative intensity	SBR	SNR
Sb I 252.852	252.860	0.684	5.6	26.5
Sb I 259.805	259.805	1.000	8.7	39.6
Sb I 276.993	276.995	0.345	2.9	11.2
Sb I 287.792	287.795	0.551	4.2	18.7
Sb I 302.983	302.990	0.238	1.9	5.7
Sb I 323.252	323.255	0.555	4.1	21.8
Sb I 326.751	326.750	0.618	4.6	25.3
Sb I 363.785	363.785	0.185	1.6	5.2
Cl I 725.662	725.675	0.202	3.1	8.7
Cl I 774.497	774.515	0.132	2.5	13.8
Cl I 821.204	821.210	0.127	2.5	17.1
Cl I 833.331	833.345	0.188	4.3	24.8
Cl I 857.524	857.525	0.152	3.5	9.7
Cl I 858.597	858.605	0.301	6.7	38.2
Cl I 894.806	894.815	0.247	6.4	29.5
Cl I 919.173	919.190	0.076	4.3	26.0

LIBS measurements were also conducted in $SbCl_5$ vapor for the first time. In these measurements, both spectrometers were used to capture the entire spectral region during a series of different experiments. Fig. 8a and b show spectra acquired using the two different spectrometers, one with a range from 200–1000 nm and the other with a range from 350–950 nm. The spectra were analyzed, and spectral peaks were identified for Sb, Cl, N, H, and O lines. The presence of N, O, and H indicate that some air infiltrated the cell, most likely due to the leaky seals of the optical cell. For data shown in Fig. 8a, the laser energy was 28 mJ with a gate delay of 3 μs, and each spectrum was an accumulation of 20 laser shots at a frequency of 3.33 Hz. For the spectra shown in Fig. 8a, spectral lines were identified for Sb and Cl as tabulated in Table 3. The strongest Sb line, at 259.805 nm has a SBR of 8.7 and a SNR of 39.6, indicating that it could be used for quantitative analysis. From previous gas phase work, the Sb I 252.852 nm line was used effectively to generate calibration curves.[41]

Table 4 Spectral lines for $SbCl_5$ observed using the 350–950 nm spectrometer. The intensity is shown relatively to the strongest Cl line

Spectral line (nm)	Wavelength (nm)	Relative intensity	SBR	SNR
Sb I 363.785	363.776	0.69	5.8	6.1
Cl I 725.662	725.654	0.48	40.0	32.8
Cl I 754.707	754.698	0.30	11.7	11.2
Cl I 774.497	774.486	0.26	9.6	11.9
Cl I 821.204	821.194	0.13	13.5	9.5
Cl I 833.331	833.334	0.29	16.0	14.0
Cl I 837.594	837.580	1.00	65.8	43.3
Cl I 842.825	842.814	0.63	1.3	8.7
Cl I 857.524	857.506	0.20	34.6	29.1
Cl I 858.597	858.584	0.40	237.4	51.6
Cl I 894.806	894.796	0.35	45.9	30.9
Cl I 907.317	907.298	0.12	7.8	6.0
Cl I 912.115	912.108	0.87	2.3	7.1
Cl I 919.173	919.166	0.16	28.3	43.2

The data presented in Fig. 8b was collected using a laser energy of 26 mJ with a gate delay of 2 μs, and each spectrum is an accumulation of 120 shots taken at 2 Hz. In this spectral range, only one Sb line was identified at 363.785 nm with a SNR of 6.1, though several strong chloride lines were identified in the spectra. Additionally, prominent N and O lines were identified along with a weak H line at 656.27 nm. Table 4 lists Sb and Cl lines identified in the spectra using the spectral range 350–950 nm. The Sb lines reported here are consistent with other ref. 38–42 and 55 for Sb, though to our knowledge this is the first time LIBS was performed in a $SbCl_5$ gas phase.

As part of one of the $SbCl_5$ experiments using the spectrometer with a range of 350–950 nm, a gate delay study was conducted in which the gate delay was varied between 1–25 μs. For each gate delay value, 5–6 replicate measurements were taken, and from each replicate, the SBR, SNR, and intensity of several peaks were calculated and averaged. These values were then averaged across the replicates. Fig. 9 shows the average SBR, SNR, and intensities of the Cl I 837.594 nm, Sb I 363.785 nm, Ar I 763.51 nm, and O I 777.19 nm lines. The error bars represent the standard deviations between the different replicates, which tended to be high relative to the variation caused by different gate delays. For all four elements of interest, the peak intensity decreased with increasing gate delay, as expected. For Cl, the SBR and SNR did not change significantly as a function of gate delay. For Sb, there is a slight maximum in the SNR and in the SBR at 15 μs gate delay, but due to the high variance between repetitions, the maximum may not be statistically significant. Similarly, for the O line, there is a maximum in the SBR at 20 μs, but not for the SNR. However, for Ar, there is a statistically significant peak at 10 μs. Therefore, selecting longer gate delays appears to be advantageous in these gas phase experiments.

Post-experiments, a deposition and some etching on the the windows was observed. The window temperatures were too hot for $SbCl_5$ to condense or freeze. Consequently, a thermodynamic assessment of potential $SbCl_5$ reactions with O_2 or H_2O as contaminants in the cell using HSC Chemistry software[44] was performed, which indicates that the reaction of $SbCl_5$ with oxygen is thermodynamically unfavorable at all temperatures. However, in the presence of moisture (H_2O), $SbCl_5$ can form

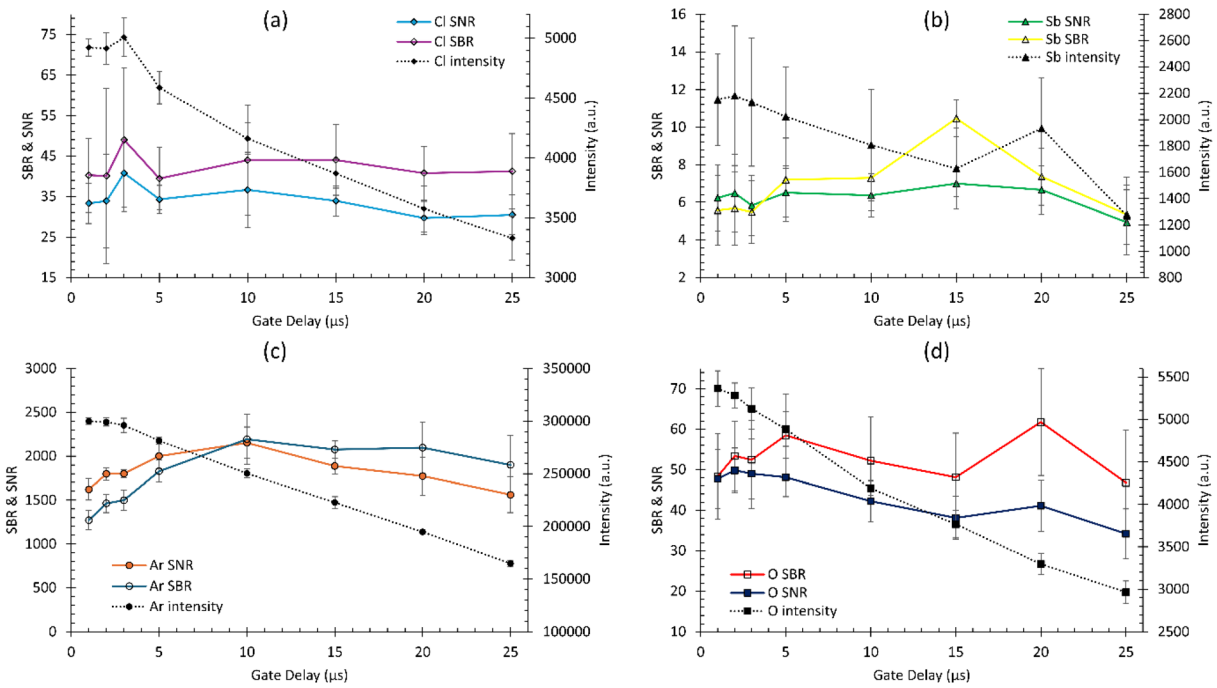

Fig. 9 Results from the gate delay optimization study. (a) The Cl I 837.594 nm line, (b) Sb I 363.785 nm line, (c) the Ar I 763.51 nm line, and (d) the O I 777.19 nm line.

Sb_2O_5 and HCl at temperatures between 300–400 °C. The reaction is as follows:

$$2SbCl_5\ (g) + 5H_2O\ (g) = Sb_2O_5\ (s) + 10HCl\ (g)$$

Based on LIBS results, O, N, and H were present despite purging with argon gas. As a result, it is likely that H_2O was present in the cell (either initially or *via* leakage) to react with $SbCl_5$. Thus, the deposition on the windows was likely Sb_2O_5 and the observed etching might have been caused by HCl in the optical cell.

4 Conclusions

A modular design of the optical cell that allows for the optimization of optical path length and beam diameter, accommodating the distinct requirements of each spectroscopy approach, has been presented. The design and development of this novel optical cell presents a significant advancement in the field of high-temperature vapor phase spectroscopy. The integration of UV-vis and LIBS spectroscopy into a single, versatile apparatus provides a powerful tool for comprehensive chemical analysis of vapor phase species. The limitation of initial design was condensation of test species on the optical windows, which was addressed by implementing a cover gas buffer on the window. This innovative feature effectively prevents material buildup, ensuring the integrity and longevity of the cell during extended operation. The successful application of this cell in analyzing both organic (naphthalene) and inorganic ($SbCl_5$) vapors highlights its potential in various scientific and industrial applications, including environmental monitoring, pharmaceuticals, materials science, and chemical manufacturing. The modular and adaptable nature of the optical cell ensures that it can meet diverse needs of various scientific and industrial applications, paving the way for future research and development in the field of vapor phase spectroscopy. This work sets a foundation for further explorations into combining multiple spectroscopy techniques within a single apparatus, offering a comprehensive tool for advanced chemical analysis in complex environments. The introduction of the cover gas buffer further enhances the cell's capability, making it a robust solution for high-temperature vapor phase analysis.

Data availability

Data used to generate plots, figures, and tables are available on the INL BOX account *via* the URL below: **https://inlbox.box.com/s/oqovrxgt5iumuv3knettw7hrwitwqwm0**.

Author contributions

Robin Roper: conceptualization (supporting), methodology (equal), investigation (equal), writing – original draft (equal), writing – review & editing (supporting). Ruchi Gakhar: funding acquisition (supporting), supervision (equal), conceptualization (supporting), methodology (equal), formal analysis (equal), investigation (equal), writing – original draft (equal), writing – review & editing (leading). Alejandro Ramos Ballesteros: methodology (supporting), formal analysis (equal), writing – review & editing (supporting). Ammon Williams: funding acquisition (lead), project administration (lead), supervision (equal), conceptualization (lead), methodology (equal), formal analysis (equal), investigation (equal), writing – original draft (equal), writing – review & editing (supporting).

Conflicts of interest

There are no conflicts to declare.

Acknowledgements

Funding for this work was primarily provided by the U.S. Department of Energy's Advanced Research Projects Agency-Energy (ARPA-E) under Award Number DE-AR0001612. Work was also partially supported through the Idaho National Laboratory Directed Research & Development (LDRD) Program under DOE Idaho Operations Office Contract DE-AC07-05ID14517.

References

1 Y. Guo, C. Liu, R. Ye and Q. Duan, Advances on Water Quality Detection by UV-vis Spectroscopy, *Appl. Sci.*, 2020, **10**(19), 6874, DOI: **10.3390/app10196874**.
2 F. S. Rocha, A. J. Gomes, C. N. Lunardi, S. Kaliaguine and G. S. Patience, Experimental Methods in Chemical Engineering: Ultraviolet Visible Spectroscopy—UV-vis, *Can. J. Chem. Eng.*, 2018, **96**(12), 2512–2517, DOI: **10.1002/cjce.23344**.
3 D. Kirsanov, A. Rudnitskaya, A. Legin and V. Babain, UV-vis Spectroscopy with Chemometric Data Treatment: An Option for on-Line Control in Nuclear Industry, *J. Radioanal. Nucl. Chem.*, 2017, **312**(3), 461–470, DOI: **10.1007/s10967-017-5252-8**.
4 G. Kaur, H. Singh and J. Singh, UV-vis Spectrophotometry for Environmental and Industrial Analysis, in *Green Sustainable Process for Chemical and Environmental Engineering and Science*, Elsevier, 2021, pp 49–68.
5 S. N. Thakur and J. P. Singh, Fundamentals of LIBS and Recent Developments, *Laser Induced Breakdown Spectrosc.*, 2020, 3–22.
6 Y. Zhang, T. Zhang and H. Li, Application of Laser-Induced Breakdown Spectroscopy (LIBS) in Environmental Monitoring, *Spectrochim. Acta, Part B*, 2021, **181**, 106218.
7 J. Naozuka and A. P. Oliveira, *Laser-Induced Breakdown Spectroscopy (LIBS) in Forensic Sensing*, 2019.
8 R. Noll, H. Bette, A. Brysch, M. Kraushaar, I. Mönch, L. Peter and V. Sturm, Laser-Induced Breakdown Spectrometry—Applications for Production Control and Quality Assurance in the Steel Industry, *Spectrochim. Acta, Part B*, 2001, **56**(6), 637–649.
9 R. Agrawal, R. Kumar, S. Rai, A. K. Pathak, A. K. Rai and G. K. Rai, LIBS: A Quality Control Tool for Food

Supplements, *Food Biophys.*, 2011, **6**(4), 527–533, DOI: 10.1007/s11483-011-9235-y.

10 P. K. Tiwari, S. Awasthi, R. Kumar, R. K. Anand, P. K. Rai and A. K. Rai, Rapid Analysis of Pharmaceutical Drugs Using LIBS Coupled with Multivariate Analysis, *Laser Med. Sci.*, 2018, **33**(2), 263–270, DOI: 10.1007/s10103-017-2358-8.

11 J. Wu, Y. Qiu, X. Li, H. Yu, Z. Zhang and A. Qiu, Progress of Laser-Induced Breakdown Spectroscopy in Nuclear Industry Applications, *J. Phys. D: Appl. Phys.*, 2019, **53**(2), 023001.

12 J. P. Singh, F.-Y. Yueh, H. Zhang and K. P. Karney, A Preliminary Study of the Determination of Uranium, Plutonium and Neptunium by Laser-Induced Breakdown Spectroscopy, *Recent Res. Dev. Appl. Spectrosc.*, 1999, **2**, 59–67.

13 E. J. Judge, J. E. Barefield, J. M. Berg, S. M. Clegg, G. J. Havrilla, V. M. Montoya, L. A. Le and L. N. Lopez, Laser-Induced Breakdown Spectroscopy Measurements of Uranium and Thorium Powders and Uranium Ore, *Spectrochim. Acta, Part B*, 2013, **83–84**, 28–36, DOI: 10.1016/j.sab.2013.03.002.

14 J. E. Barefield, E. J. Judge, J. M. Berg, S. P. Willson, L. A. Le and L. N. Lopez, Analysis and Spectral Assignments of Mixed Actinide Oxide Samples Using Laser-Induced Breakdown Spectroscopy (LIBS), *Appl. Spectrosc.*, 2013, **67**(4), 433–440, DOI: 10.1366/12-06830.

15 C. A. Smith, M. A. Martinez, D. K. Veirs and D. A. Cremers, Pu-239/Pu-240 Isotope Ratios Determined Using High Resolution Emission Spectroscopy in a Laser-Induced Plasma, *Spectrochim. Acta, Part B*, 2002, **57**(5), 929–937, DOI: 10.1016/S0584-8547(02)00023-X.

16 F. R. Doucet, G. Lithgow, R. Kosierb, P. Bouchard and M. Sabsabi, Determination of Isotope Ratios Using Laser-Induced Breakdown Spectroscopy in Ambient Air at Atmospheric Pressure for Nuclear Forensics, *J. Anal. At. Spectrom.*, 2011, **26**(3), 536–541, DOI: 10.1039/c0ja00199f.

17 C. Dumitrescu, P. Puzinauskas, S. Olcmen, S. G. Buckley, S. Joshi and A. P. Yalin, Fiber-Optic Spark Delivery for Gas-Phase Laser-Induced Breakdown Spectroscopy, *Appl. Spectrosc.*, 2007, **61**(12), 1338–1343, DOI: 10.1366/000370207783292217.

18 C. A. Henry, P. K. Diwakar and D. W. Hahn, Investigation of Helium Addition for Laser-Induced Plasma Spectroscopy of Pure Gas Phase Systems: Analyte Interactions and Signal Enhancement, *Spectrochim. Acta, Part B*, 2007, **62**(12), 1390–1398, DOI: 10.1016/j.sab.2007.10.002.

19 G. C. Y. Chan, L. R. Martin, L. D. Trowbridge, Z. Zhu, X. Mao and R. E. Russo, Analytical Characterization of Laser Induced Plasmas towards Uranium Isotopic Analysis in Gaseous Uranium Hexafluoride, *Spectrochim. Acta, Part B*, 2021, **176**, 106036, DOI: 10.1016/j.sab.2020.106036.

20 G. C. Y. Chan, L. R. Martin and R. E. Russo, Characterization and Optimization of a Spectral Window for Direct Gaseous Uranium Hexafluoride Enrichment Assay Using Laser-Induced Breakdown Spectroscopy, *Appl. Spectrosc.*, 2022, 1–16, DOI: 10.1177/00037028221112953.

21 G. C. Y. Chan, X. Mao, L. R. Martin, L. D. Trowbridge and R. E. Russo, Direct Uranium Enrichment Assay in Gaseous Uranium Hexafluoride with Laser Induced Breakdown Spectroscopy, *J. Radioanal. Nucl. Chem.*, 2022, **331**(3), 1409–1421, DOI: 10.1007/s10967-022-08215-2.

22 C. Haisch, Element-Specific Determination of Chlorine in Gases by Laser-Induced-Breakdown-Spectroscopy (LIBS), *Fresenius' J. Anal. Chem.*, 1996, **356**(1), 21–26, DOI: 10.1007/s0021663560021.

23 M. Hanafi, M. M. Omar and Y. E. E. D. Gamal, Study of Laser-Induced Breakdown Spectroscopy of Gases, *Radiat. Phys. Chem.*, 2000, **57**(1), 11–20, DOI: 10.1016/S0969-806X(99)00344-8.

24 C. G. Morgan, Laser-Induced Breakdown of Gases, *Rep. Prog. Phys.*, 1975, **38**(5), 621–665, DOI: 10.1088/0034-4885/38/5/002.

25 C. W. Dekock and D. M. Gruen, Electronic Absorption Spectra of the Gaseous 3d Transition-Metal Dichlorides, *J. Chem. Phys.*, 1966, **44**(12), 4387–4398, DOI: 10.1063/1.1740008.

26 D. M. Gruen and R. L. McBeth, Vapor Complexes of Uranium Pentachloride and Uranium Tetrachloride with Aluminum Chloride. The Nature of Gaseous Uranium Pentachloride, *Inorg. Chem.*, 1969, **8**(12), 2625–2633, DOI: 10.1021/ic50082a017.

27 H. A. Oye and D. M. Gruen, Neodymium Chloride-Aluminum Chloride Vapor Complexes, *J. Am. Chem. Soc.*, 1969, **91**(9), 2229–2236, DOI: 10.1021/ja01037a008.

28 S. Boghosian and G. N. Papatheodorou, Halide Vapors and Vapor Complexes, *Handbook on the Physics and Chemistry of Rare Earths*, 2001, vol. 23, ch. 1996, pp. 435–496.

29 G. N. Papatheodorou and G. H. Kucera, Vapor Complexes of Samarium(III) and Samarium(II) Chlorides with Aluminum(III) Chloride, *Inorg. Chem.*, 1979, **18**(2), 385–389, DOI: 10.1021/ic50192a038.

30 H. A. Doerner, *Chemistry of the Anhydrous Chlorides of Chromium; Technical Paper 577*, U.S. Bur. Mines, 1937.

31 C. Beusman, *Activities in the KCl-FeCh and LiCl-FeCh Systems; Report 2323*, Oak Ridge National Laboratory, 1957.

32 J. Sime and N. W. Gregory, Vapor Pressures of FeCl2, FeBr2, and FeI2 by the Torsion Effusion Method, *J. Phys. Chem.*, 1960, **64**, 86.

33 H. Schafer, L. Bayer, G. Breil, K. Etzel and K. Krehl, Saturation Pressures of Manganese Chloride, Ferrous Chloride, Cobaltous Chloride, and Nickel Chloride, *Z. Anorg. Allg. Chem.*, 1955, **278**, 300–309.

34 J. T. Hougen, G. E. Leroi and T. C. James, Application of Ligand Field Theory to the Electronic Spectra of Gaseous $CuCl_2$, $NiCl_2$, and $CoCl_2$, *J. Chem. Phys.*, 1961, **34**(5), 1670–1677, DOI: 10.1063/1.1701063.

35 D. M. Gruen and H. A. Øye, Vapor Complex of Neodymium Chloride with Aluminum Chloride, *Inorg. Nucl. Chem. Lett.*, 1967, **3**(10), 453–455, DOI: 10.1016/0020-1650(67)80104-1.

36 D. M. Gruen and C. W. DeKock, Absorption Spectra of Gaseous $NdBr_3$ and NdI_3, *J. Chem. Phys.*, 1966, **45**, 455.

37 N. W. Gregory, UV-Vis Vapor Absorption Spectrum of Antimony(III) Chloride, Antimony(v) Chloride, and Antimony(III) Bromide. The Vapor Pressure of Antimony(III)

Bromide, *J. Chem. Eng. Data*, 1995, **40**(4), 963–967, DOI: 10.1021/je00020a051.

38 M. Stepputat and R. Noll, On-Line Detection of Heavy Metals and Brominated Flame Retardants in Technical Polymers with Laser-Induced Breakdown Spectrometry, *Appl. Opt.*, 2003, **42**(30), 6210–6220, DOI: 10.1364/AO.42.006210.

39 H. Fink, U. Panne and R. Niessner, Analysis of Recycled Thermoplasts from Consumer Electronics by Laser-Induced Plasma Spectroscopy, *Anal. Chim. Acta*, 2001, **440**(1), 17–25, DOI: 10.1016/S0003-2670(00)01357-X.

40 S. Ü. Yeşiller and Ş. Yalçın, Optimization of Chemical and Instrumental Parameters in Hydride Generation Laser-Induced Breakdown Spectrometry for the Determination of Arsenic, Antimony, Lead and Germanium in Aqueous Samples, *Anal. Chim. Acta*, 2013, **770**, 7–17.

41 J. B. Simeonsson and L. J. Williamson, Characterization of Laser Induced Breakdown Plasmas Used for Measurements of Arsenic, Antimony and Selenium Hydrides, *Spectrochim. Acta, Part B*, 2011, **66**(9–10), 754–760.

42 V. Lazic, M. Filella and A. Turner, Determination of Antimony Concentrations in Widely Used Plastic Objects by Laser Induced Breakdown Spectroscopy (LIBS), *J. Anal. At. Spectrom.*, 2018, **33**(11), 1917–1924, DOI: 10.1039/c8ja00181b.

43 J. Ferguson, L. W. Reeves and W. G. Schneider, Vapor Absorption Spectra and Oscillator Strengths of Naphthalene, Anthracene, and Pyrene, *Can. J. Chem.*, 1957, **35**(10), 1117–1136.

44 HSC Chemistry, https://www.hsc-chemistry.com/hscchemistry, accessed 2024-12-19.

45 G. A. George and G. C. Morris, The Intensity of Absorption of Naphthalene from 30 000 cm^{-1} to 53 000 cm^{-1}, *J. Mol. Spectrosc.*, 1968, **26**(1), 67–71.

46 M. Suto, X. Wang, J. Shan and L. C. Lee, Quantitative Photoabsorption and Fluorescence Spectroscopy of Benzene, Naphthalene, and Some Derivatives at 106–295 nm, *J. Quant. Spectrosc. Radiat. Transfer*, 1992, **48**(1), 79–89.

47 M. Orain, P. Baranger, B. Rossow and F. Grisch, Fluorescence Spectroscopy of Naphthalene at High Temperatures and Pressures: Implications for Fuel-Concentration Measurements, *Appl. Phys. B:Lasers Opt.*, 2011, **102**, 163–172.

48 H. Grosch, Z. Sárossy, H. Egsgaard and A. Fateev, UV Absorption Cross-Sections of Phenol and Naphthalene at Temperatures up to 500 °C, *J. Quant. Spectrosc. Radiat. Transfer*, 2015, **156**, 17–23, DOI: 10.1016/j.jqsrt.2015.01.021.

49 E. Clar, Absorption Spectra of Aromatic Hydrocarbons at Low Temperatures. LV-Aromatic Hydrocarbons, *Spectrochim. Acta*, 1950, **4**(2), 116–121, DOI: 10.1016/S0371-1951(50)80005-X.

50 J. G. Angus and G. C. Morris, Naphthalene-Rare Gas Solids: Absorption Spectra from 30 000–30 000 cm^{-1}, *Mol. Cryst. Liq. Cryst.*, 1970, **11**(3), 257–277, DOI: 10.1080/15421407008083518.

51 E. N. Rao, P. Mathi, S. A. Kalam, S. Sreedhar, A. K. Singh, B. N. Jagatap and S. V. Rao, Femtosecond and Nanosecond LIBS Studies of Nitroimidazoles: Correlation between Molecular Structure and LIBS Data, *J. Anal. At. Spectrom.*, 2016, **31**(3), 737–750.

52 S. J. Mousavi, M. Hemati Farsani, S. M. R. Darbani, N. Asadorian, M. Soltanolkotabi and A. Eslami Majd, Identification of Atomic Lines and Molecular Bands of Benzene and Carbon Disulfide Liquids by Using LIBS, *Appl. Opt.*, 2015, **54**(7), 1713–1720.

53 S. Paul, B. Sen, N. Chakraborty, S. Das, S. Mondal, A. P. Chattopadhyay and S. I. Ali, pH-Regulated Hydrothermal Synthesis and Characterization of $Sb_4O_5X_2$ (X = Br/Cl) and Its Use for the Dye Degradation of Methyl Orange Both with and without Light Illumination, *RSC Adv.*, 2022, **12**(14), 8374–8384, DOI: 10.1039/d2ra01215d.

54 C. Hu, D. Chu, X. Hou, F. Zhang and J. Han, Exploration of Antimony(III) Oxyhalides *via* Single-Site Substitution in Quest of Large Birefringence, *Inorg. Chem. Front.*, 2024, **11**(11), 3367–3376, DOI: 10.1039/d4qi00564c.

55 Libs-info Element Sb, https://libs-info.com/element/Sb/, accessed 2024-12-18.